Spiderweb Nanomechanical Resonators via Bayesian Optimization: Inspired by Nature and Guided by Machine Learning

Dongil Shin, Andrea Cupertino, Matthijs H. J. de Jong, Peter G. Steeneken, Miguel A. Bessa,* and Richard A. Norte*

From ultrasensitive detectors of fundamental forces to quantum networks and sensors, mechanical resonators are enabling next-generation technologies to operate in room-temperature environments. Currently, silicon nitride nanoresonators stand as a leading microchip platform in these advances by allowing for mechanical resonators whose motion is remarkably isolated from ambient thermal noise. However, to date, human intuition has remained the driving force behind design processes. Here, inspired by nature and guided by machine learning, a spiderweb nanomechanical resonator is developed that exhibits vibration modes, which are isolated from ambient thermal environments via a novel "torsional soft-clamping" mechanism discovered by the data-driven optimization algorithm. This bioinspired resonator is then fabricated, experimentally confirming a new paradigm in mechanics with quality factors above 1 billion in room-temperature environments. In contrast to other state-of-the-art resonators, this milestone is achieved with a compact design that does not require sub-micrometer lithographic features or complex phononic bandgaps, making it significantly easier and cheaper to manufacture at large scales. These results demonstrate the ability of machine learning to work in tandem with human intuition to augment creative possibilities and uncover new strategies in computing and nanotechnology.

1. Introduction

Major advances in nanotechnology have allowed mechanical resonators to improve dramatically over the last decades. One of the most sought after characteristics for a mechanical resonator is noise isolation from thermal environments, namely at room-temperature conditions where thermomechanical noise can dominate. The degree of mechanical isolation is characterized by a resonator's mechanical quality factor, Q_m. Typically, Q_m is defined as the ratio of energy stored in a resonator over the energy dissipated over one cycle of oscillation. Inversely, mechanical quality factors can indicate the dissipation of mechanical noise into a resonator from ambient environments. For mechanical sensors, a resonator's isolation from ambient thermal noise can greatly enhance their ability to detect ultrasmall forces, pressures, positions, masses, velocities, and accelerations. For quantum technologies, mechanical quality factor dictates the average number of coherent oscillations a nanomechanical resonator (in the quantum regime) can undergo before one phonon of thermal noise enters the resonator and causes decoherence of its quantum properties.[1] From microchip sensing to quantum networks, cryogenics are conventionally required to counteract thermal noise but enabling these burgeoning technologies to operate in ambient temperatures would have a significant impact on their widespread use.

In room-temperature environments, on-chip mechanical resonators with state-of-the-art quality factors have mostly consisted of high-aspect-ratio suspended nanostructures

D. Shin, M. A. Bessa
Faculty of Mechanical
Maritime and Materials Engineering
Department of Materials Science and Engineering
Delft University of Technology
Delft 2628 CD, The Netherlands
E-mail: M.A.Bessa@tudelft.nl

The ORCID identification number(s) for the author(s) of this article can be found under https://doi.org/10.1002/adma.202106248.

D. Shin, A. Cupertino, M. H. J. de Jong, P. G. Steeneken, R. A. Norte
Faculty of Mechanical
Maritime and Materials Engineering
Department of Precision and Microsystems Engineering
Delft University of Technology
Delft 2628 CD, The Netherlands
E-mail: R.A.Norte@tudelft.nl

M. H. J. de Jong, P. G. Steeneken, R. A. Norte
Faculty of Applied Sciences
Department of Quantum Nanoscience
Kavli Institute of Nanoscience
Delft University of Technology
Delft 2628 CD, The Netherlands

**ADVANCED
SCIENCE NEWS**

www.advancedsciencenews.com

**ADVANCED
MATERIALS**

www.advmat.de

fabricated from tensile thin films. Silicon nitride (Si_3N_4) films have been the material of choice for their high intrinsic stress, yield strength, temperature stability, chemical inertness, and prevalence in nanotechnology. Over the years, researchers have developed improved design principles that manipulate the strain, bending, and mode shape in nanomechanical resonators to improve quality factors, which are ultimately limited by bending losses as the resonator oscillates in vacuum. Another important characteristic is the mechanical frequency of a nanomechanical resonator's vibrational mode, f_m. For high-precision detectors of fundamental forces like gravity and dark matter[2,3] and quantum-limited commercial sensors,[4,5] resonators with high Q_m and low f_m are a long-standing goal. Minimizing f_m/Q_m is a key figure-of-merit toward quantum-limited force[6] or acceleration[7] sensitivities ($S_f, S_a \propto (f_m/Q_m)^{0.5}$) and for enabling quantum sensing of forces like dark matter[8,9] and gravity[10,11] where low frequency and higher quality factor are advantageous. For phonon-based quantum technologies, a mechanical resonator's vibrational modes are initialized into the quantum regime, where their motion harbors less than one quanta of vibration (phonon).[12,13] Mechanical resonators in these quantum regimes must have sufficiently high $Q_m \times f_m > k_B T_{room}/h$ to suppress the effects of room temperature, T_{room}, thermal noise on their fragile quantum properties. While there are only a handful of platforms[14–21] to overcome these stringent requirements on $Q_m \times f_m$ at room temperature, a general goal has been to achieve the highest Q_m and lowest f_m possible while still maintaining $Q_m \times f_m$ above 6×10^{12} Hz.

Previously proposed nanomechanical resonators follow strategies largely motivated by 1D analytical models of resonators[23] because they provide easy-to-interpret design rules. It is important to note that while silicon nitride has been conventionally used for high-Q resonators, these design principles are valid for nearly any strained thin-film material. These analytical models show that higher strain (i.e., higher stress σ and low Young's modulus E), longer (L) and thinner (t) geometries generally lead to higher quality factors in both nanomechanical membranes and strings. For example, f_m/Q_m of the double clamped beam's fundamental mode is proportional to $\sqrt{E}/L^3$ ($L+1.4t\sqrt{E/\sigma}$), when assuming a thin long pre-stressed beam (explicit formulation can be found in the Supporting Information). While increasing the aspect-ratio of resonators usually leads to smaller f_m/Q_m, it also makes them much more challenging to fabricate reliably. **Figure 1**A illustrates conventional design strategies. When considering the fundamental mode of resonators, mechanical quality factors are typically improved by pre-stressing—a form a strain engineering called dissipation dilution[24–27] which increases stored energies and lowers dissipation compared to unstressed resonators. It overcomes the fundamental limit of the material's intrinsic damping from its bulk and surface, enabling a higher quality factor by orders of magnitude. Simultaneously, resonator models[23] also explain that for high-aspect-ratio pre-stressed resonators ($t \ll L$) the dominating loss that decreases Q_m is due to the mode's sharp curvature at the clamped boundary between the oscillating element and the substrate (on which the resonators are fabricated). This observation motivated the use of phononic crystals (i.e., phononic bandgap) which confine a higher-order mode from the clamping regions using a periodic pattern around the mode. Now rather than having large curvature near the edges, the phononic crystals enable a soft clamping[15,19,21] to reduce the mode's curvature close to the rigid clamp, and thereby eliminating this dissipation mechanism when operating at high-order vibration modes as depicted in the schematic in
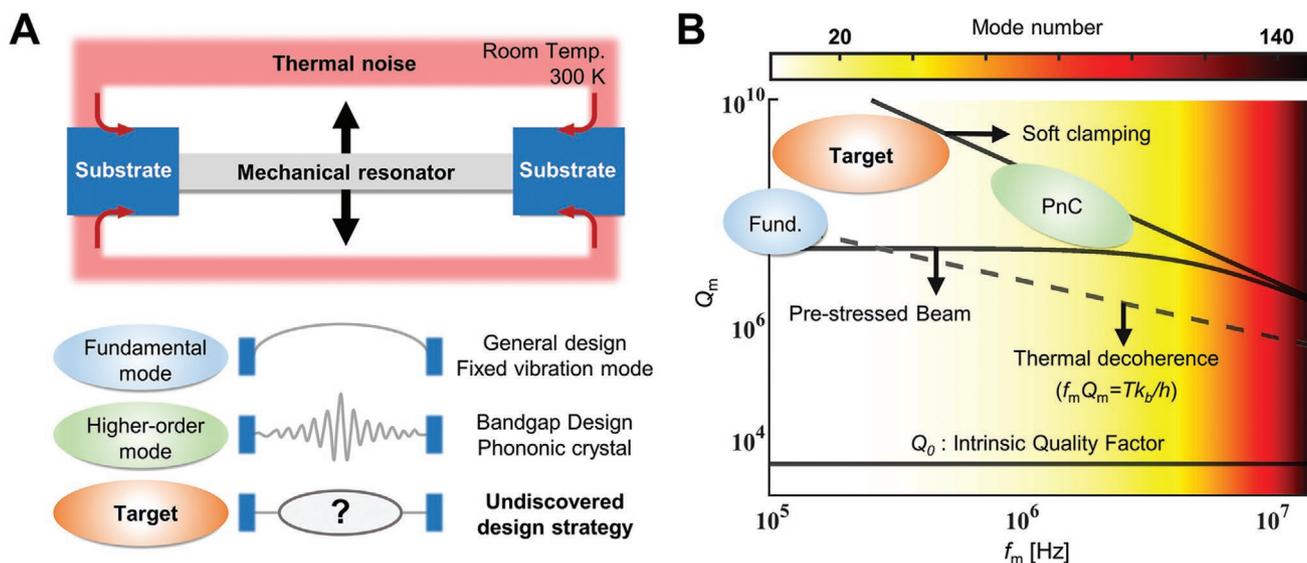

Figure 1. A) Illustration of the mechanical resonator and target vibration modes for a high-quality-factor resonator. Unlike fundamental modes,[20,22] or higher-order modes,[15] the target mode shape for lower-order mode had not been discovered. B) Quality factor (Q_m) versus frequency (f_m) for a double clamped 50 nm-thick, 3 mm-long silicon nitride beam. The bottom solid line corresponds to the intrinsic quality factor of Si_3N_4, the intermediate solid line to the effect of high pre-stress, and the upper solid line to the effect of complete elimination of clamp losses (perfect soft clamping) on the string resonator. The dashed line corresponds to the mechanical decoherence constraint, indicating that the resonator having the quality factor above can complete one full coherent oscillation without a thermal phonon entering the resonator. The figure highlights the target unexplored region of designs with high quality factors and lower-order modes.

**ADVANCED
SCIENCE NEWS**

www.advancedsciencenews.com

**ADVANCED
MATERIALS**

www.advmat.de

Figure 1A. Phononic crystals enable higher quality factors that approach hundreds of millions, at the cost of operating at higher frequencies and typically requiring higher-aspect-ratio resonators which are more difficult to manufacture reliably.

To illustrate the design space, Figure 1B shows the mechanical quality factor Q_m versus vibration frequency f_m for a 50 nm-thick and 3 mm-long Si_3N_4 beam. The color scale indicates the various out-of-plane vibration modes, from fundamental to higher-order modes with shorter wavelengths. The Supporting Information ("Lessons from string resonators") provides additional information about the bounds shown in the figure. The considered pre-stressed double clamped beam shows the improvement of Q_m caused by enhancement of stored energy (intermediate solid line) when compared to the unstressed beam (horizontal solid line at the bottom, Q_0) and the improvement caused if perfect soft clamping is achieved around the region shown in Figure 1A (top solid line). These lines help illustrate the design region in the graph's top left corner that remains largely unexplored in current resonators that aim mainly for high quality factor. Previous works have focused on increasing Q_m of the fundamental mode with strain engineering,[6,20] including design strategies as topology optimization[17,28] or hierarchical designs.[16,22] Here we pursue high quality factors at lower frequencies by following a new approach inspired by nature and guided by machine learning.

2. Results and Discussion

Spiderweb designs have unique geometries that make them one of the most well-known and fascinating classes of micromechanical structures found in nature. Despite their ubiquitous presence, experts from physics, materials science, and biology are still uncovering the elusive mechanics of spiderwebs that enable them to be remarkably robust vibration sensors.[29,30] Spider silk threads have high toughness and stiffness, reaching yield strengths of the order of a gigapascal—about five times higher than steel[31] and about the same as Si_3N_4. They are used to create lightweight fibrous web structures which harbor an extraordinary strength-to-weight ratio rarely observed among other structures found in nature or science.[32–35] Furthermore, in the case of spiders that sense their prey via webs, these structures are designed to be most sensitive to vibrations emanating from the web and not from surrounding environmental vibrational disturbances.[36–39] Since their unique sensing capabilities have been relentlessly optimized over millions of years of complex evolutionary competition,[40–42] spiderwebs stand as a promising starting point for machine-learning algorithms to design nanomechanical sensors.[43–45]

2.1. Simulation Results

Without making any assumptions about how a spiderweb functions as a vibrational sensor in nature, we propose a web-like structure composed of radial beams, lateral beams, and junctions between them, as shown in **Figure 2**. Instead of spiderweb threads which are micrometers thick, we consider highly stressed Si_3N_4 that can be as thin as 20 nm while being
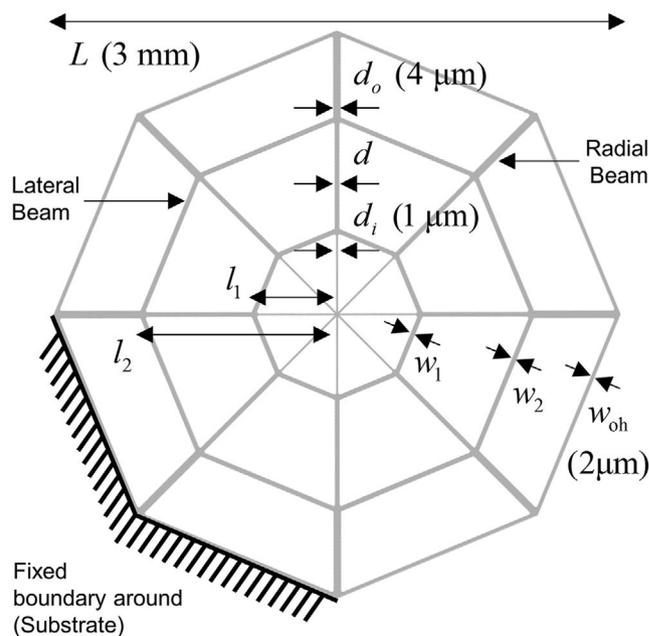

Figure 2. Spiderweb nanomechanical resonator model with $N_r = 8$. d, w_1, w_2, l_1, and l_2 are the design parameters, d_i, d_o, w_{oh}, and L are set as 1 µm, 4 µm, 2 µm, and 3 mm, respectively.

suspended over several millimeters. The properties of Si_3N_4 were considered to be $E = 250$ GPa, $v = 0.23$, $\rho = 3100$ kg m^{-3} with an initial released stress of 1.07 GPa based on measurements. The parameterized model shown in Figure 2 includes six design parameters, d, w_1, w_2, l_1, l_2, and N_r. The two inner rings (i.e., the rings formed by the lateral beams) were constrained to have at least a distance of 8 µm between them. We also considered even numbers between 4 to 16 for the number of lateral beams per ring, N_r. Note that the even number of N_r was considered to include not only the symmetric but also the antisymmetric periodic boundary condition. The beam width at the outer and inner parts of the radial beams (d_o and d_i) were taken to be 4 and 1 µm, respectively. The width of the structure at the resonator–substrate interface, w_{oh}, was set to 2 µm (half the maximum beam width) in the finite element model to reflect the inevitable overhang originating from the fabrication process. The fixed boundary condition around the resonator is modeled to reflect the overhang attached to a fixed substrate. Additionally, we gave a 1 µm radius fillet for every corner at the junction of lateral and radial beams. By limiting the model's features such as tether widths and fillets to micrometer scales (rather than sub-micrometer), it ensures that these structures can ultimately be defined using photolithography which allow for significantly easier, large-scale fabrication. Finally, the simulation model in the paper considers L, t as 3 and 50 nm, respectively. From the simulation, we estimated the mechanical quality factor of the resonator by calculating the dissipation dilution[27,46] of the out-of-plane vibration modes. The quality factors are calculated as,

$$\frac{Q_m}{Q_0} = \frac{12(1-v^2)}{Et^2} \frac{\int \alpha dS}{\int \beta dS} \tag{1}$$

with α and β being defined as,

**ADVANCED
SCIENCE NEWS**

www.advancedsciencenews.com

**ADVANCED
MATERIALS**

www.advmat.de

$$\alpha = \sigma_{xx} u_{z,x}^2 + \sigma_{yy} u_{z,y}^2 + 2\sigma_{xy} u_{z,x} u_{z,y} \qquad (2)$$

$$\beta = u_{z,xx}^2 + u_{z,yy}^2 + 2\nu u_{z,xx} u_{z,yy} + 2(1-\nu) u_{z,xy}^2 \qquad (3)$$

with u_z being the out-of-plane displacement during vibration, and σ the stress distribution resulting from static analysis for the initial stress. The comma denotes a partial derivative with respect to that coordinate. Q_0 is the intrinsic quality factor defined as $Q_0^{-1} = Q_{volume}^{-1} + Q_{surface}^{-1}$, where Q_{volume} is the bulk material loss of Si_3N_4, and $Q_{surface}$ is the surface loss that varies linearly with the resonator's thickness. For thin resonators at room temperature, we assume $Q_0 \approx 6900t/100$ nm.[47] Note that α is proportional to the elastic energy in tension, which corresponds to the energy stored in the resonator, and β is proportional to the bending loss. The detailed derivation is provided in the Supporting Information ("Derivation of the quality factor for two-dimensional structures"). With the parameterized model, we aimed to find the highest quality factor considering general types of mode shape below 1 MHz, which is the tenth mode frequency of the same size of the pre-stressed string in Figure 1B. Given that the length L of our spiderweb nanomechanical resonators are limited to 3 mm, this ensures a target frequency in the hundreds of kHz regime.

The choice of optimization algorithm to guide the data-driven design process represents the most crucial part for solving real application problems and depends on the characteristics of the problem and data availability. For example, recently machine-learning algorithms have proved their success in material design problems with abundant data.[48–50] On the contrary in this case, a new resonator is designed based on a new spiderweb model shown in Figure 2 and therefore, no prior data is available. Trial-and-error experimentation is difficult because conducting a single experiment of a particular design takes several days of fabrication and testing. In addition, fast analytical predictions of the quality factors and vibrational mode frequencies of designs are also not possible due to the complexity of the 2D geometry, which also requires to consider various vibration mode shapes. In fact, finite element analyses of these structures are computationally expensive; taking between 10 and 30 minutes using 20 CPU cores of our high performance computing cluster. Despite only considering periodic boundary conditions and simulating only a fraction of the total structure, these long simulation times arise from the fine mesh of elements required by the high-aspect-ratio structure such that the subtle shape curvatures are captured in small but crucial regions, such as joints. The geometry is meshed with 4 to 6 elements in the beam's width direction using shell elements, and the mesh resolution near the joints is about double that (details of the finite element model information can be found in the Supporting Information). Therefore, a week of computation can only generate data corresponding to less than 1000 design iterations. This is then classified as a data-scarce optimization problem where each new design iteration should be as informative to the design goal as possible. Under these conditions, using data-scarce machine learning to guide the optimization process is particularly effective, as achieved by the Bayesian optimization method.[51–53]

Bayesian optimization[54] constructs a machine-learning regression model usually from Gaussian processes,[55] by predicting model uncertainty and seeking the optimum solution in fewer iterations than competing algorithms.[56,57] Applying the algorithm to new problem domains, which requires new kinds of surrogate models without pre-domain knowledge as in our problem, is especially beneficial.[57] For readers unfamiliar with the topic, the Supporting Information includes a short introduction to the method. In the context of designing the spiderweb nanomechanical resonator, Bayesian optimization is expected to not only explore the design space to find new vibrational modes that induce soft clamping with a compact design, but also use them to reach high quality factors in the low frequency regime for a given resonator size. In this work, we used the GPyOpt Python implementation of the method,[58] and MATLAB for the pre- and post-processing of our spiderweb design. The finite element analysis was performed by COMSOL.[59]

Figure 3 refers to the optimization history wherein the spiderweb nanomechanical resonator's quality factor is maximized. The process starts with a random search of 40 iterations to train the model (shown in light blue), followed by the Bayesian optimization phase (shown in light red). Figure 3B shows the evolution of the quality factor Q_m, while Figure 3D plots the distance from a previous optimized point to the point considered in that iteration (the distance between the normalized input vectors). As seen in Figure 3A, the random search from iterations 1–40 find vibrational modes with the highest quality factors in iteration 26 and 27 which vibrate in the outer lateral ring. When the Bayesian optimization starts at iteration 41 (red markers), it begins to follow the vibrational modes concentrated on the inner lateral beams. Even though iteration 41 starts with a quality factor similar to the one found in the random search (light blue region), the algorithm continues exploiting the optimal design region without going too far from this successful iteration, as can be seen in Figure 3D between iterations 41 and 51, mostly by finely tuning design parameters as can be seen in Figure 3E. In these iterations, the design improves the quality factor by more than 180% compared to the best value obtained from the first 40 random searches and the machine-learning model promotes local optimization.

Note that the optimal modes found during the Bayesian optimization process correspond to vibrational modes (iterations 41, 51, 136 in Figure 3A) which harbor only a slight deformation near the clamping points because the major bending elements are in the intermediate ring. Surprisingly, these lateral vibrational modes mimic actual vibrations utilized in spiderwebs for prey detection.[60] Without encoding any prior knowledge about how spiderwebs function, the machine-learning algorithm was able to find how actual spiderwebs work in nature and adapt it to silicon nitride nanostructures. After iteration 51, the algorithm starts exploring the design space more to search for a better design far from the previous optimal, which can be seen from the high values in Figure 3D. This trade-off between exploration and exploitation is often responsible for the competitive advantage of Bayesian optimization when compared to other algorithms. The green markers in Figure 3 are clear examples of the Bayesian optimization exploring far from previous optima. Note that the lateral beam's vibrational mode did not always have the highest quality factor, as optimum
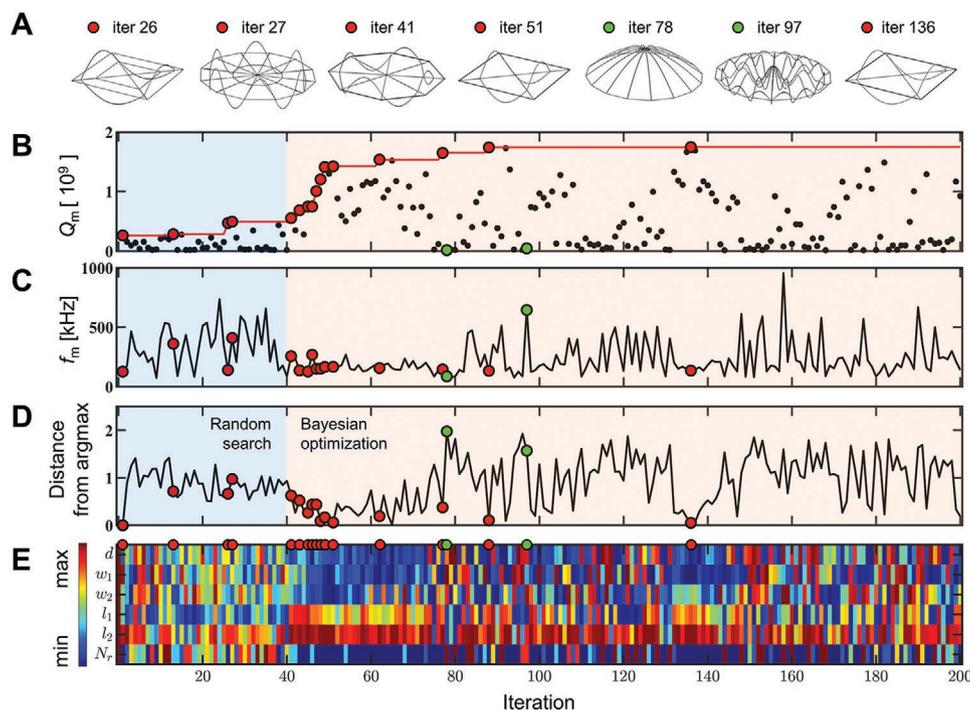
Figure 3. Overview of the Bayesian optimization process for designing the spiderweb nanomechanical resonator: A) designs and simulated mode shapes at the corresponding iterations highlighted by circular markers in the remaining figures (the enlarged figures are in the Supporting Information). B) Evolution of the quality factor Q_m (the red markers and red line indicate the highest quality factor until that iteration). C) The frequency f_m. D) The distance from a previous optimized point to the point considered in that iteration. E) Values of the six design parameters at every iteration, providing an idea of how the designs change in the optimization process ($4 \leq N_r \leq 16$, $1\,\mu m \leq (d, w_1, w_2) \leq 4\,\mu m$, $0\,mm < l_1 < l_2 < 1.5\,mm$). The abscissa for (B)–(E) is the same and corresponds to the design iterations as the optimization process evolves. The blue region in (B)–(D) corresponds to the 40 initial designs that were randomly selected, that is, before starting the Bayesian optimization process; while the red region corresponds to the Bayesian optimization iterations.

performance arises from the discovery of this new mode in combination with geometric parameters that promote bending and torsion in a particular way, as discussed later. By exploring and exploiting simultaneously to optimize the quality factor of the mechanical resonator, the algorithm reaches a maximum quality factor in iteration 136. Bayesian optimization consistently balances exploitation and exploration, so the solution for a large number of iterations could lead to continuous improvement. The result here considers up to 200 iterations for the optimization, considering a few days for optimization. In the case of having thousands of data sets regardless of the computational cost, the consideration of additional design parameters could be interesting for future work. As seen in Figure 3C, we also found that the highest quality factors Q_m occur at lower frequencies, which agrees with the simplified 1D model of the beam resonator. Note that the convergence speed and the optimum result could depend on the initial searching points. The comparison study can be found in the Supporting Information ("Optimization convergence dependency on the initial random points"). Moreover, the optimization process also shows that thinner structures are not necessarily better when using micro-wide tethers—a counter-intuitive finding given that every previous design of nanomechanical resonators had out-of-plane mechanical modes with Q_m that benefited from thinner geometries. The detailed discussion can be found in the Supporting Information ("Conversion of energy loss

regarding the thickness of the spiderweb nanomechanical resonator").

The optimum spiderweb nanomechanical resonator is predicted to have a quality factor Q_m above 1.75 billion at 134.9 kHz for a design considering a diagonal size of 3 mm and a thickness of 50 nm. **Table 1** shows the design parameters corresponding to this design. Comparatively, what is striking about this design is that it is able to achieve a quality factor Q_m above a billion without requiring any tether widths under a micrometer. This allows it to be readily defined using large-scale photolithography which further makes manufacturing faster and cheaper. This is extremely beneficial for real applications in that it decreases the resonators' microchip footprint. For thermal management, lower aspect ratio is very beneficial as typically Si_3N_4 nanoresonators are interfaced with optics for high-precision sensing and quantum application. Although Si_3N_4 is preferred for its low optical absorption,[26,61] even small amounts of optical heating can have deleterious consequences for high-precision experiments, and having a smaller aspect ratio allows for

Table 1. Optimal design parameters for the spiderweb resonator, when d_i, d_o, w_{oh}, and L are set as 1 µm, 4 µm, 2 µm, and 3 mm, respectively.

N_r	d	w_1	w_2	l_1	l_2
4	1.05 µm	1 µm	2.46 µm	1.21 mm	1.48 mm

**ADVANCED
SCIENCE NEWS**

www.advancedsciencenews.com

**ADVANCED
MATERIALS**

www.advmat.de

enhanced thermal conduction (to the substrate) which scales as t/L. What is important to note is that previous nanomechanical resonators followed a common design paradigm wherein the maximal amplitude of the mode is in the center of the resonator and where the aim is to reduce bending losses from that center to the substrate. Here the algorithm takes an entirely different route by looking at modes that oscillate laterally like a mechanical whispering gallery mode, allowing for tiny distances between amplitude maxima and substrate, providing new insight into the nanomechanical resonator design.

Figure 4 provides additional details about the optimum design, where Figure 4A highlights the novel "torsional soft clamping" mechanism found by the data-driven strategy. This design yields an unprecedentedly high quality factor because the resonator vibrates with an out-of-plane deformation that is localized in the inner ring of lateral beams while undergoing torsional deformation of the radial beams. Figure 4B,C also support this observation, where the displacement magnitude (Figure 4B) and normalized bending loss (Figure 4C) clearly demonstrate the low displacement and bending losses at the boundary (blue marker) while the joint of the inner lateral ring (yellow marker) undergoes significant deformation. As a consequence of the radial beams' torsional motion, the curvature between the bending lateral beam with the radial beam at the clamping point is not highly concentrated, thus significantly diminishing the clamping losses at these points. Although the torsional motion of the radial beams leads to 70% of the energy dissipation, it is comparable to the bending losses in the deforming lateral beams. Note that the normalized bending loss in Figure 4C indicates that the bending energy near the joint of the inner lateral beam (yellow marker region) is spread out in the region near the joint, which avoids sharp curvatures that can ultimately limit Q_m. Additionally, the blue marker region of Figure 4A shows that the outer lateral beams near the boundary prevent deformation and bending loss from propagating toward the boundary in a subtle way by preventing torsional deformation in the radial beams from propagating to the boundary. Unlike the bending loss density of the string's bending modes[23] (where it is highly concentrated on the clamping region), the torsional bending loss density in the spiderweb resonator does not highly concentrate where the vibration stops. For this reason, simulations without the outer lateral beams also gave a similar quality factor. Nonetheless, the optimized position of the outer ring was used to block the torsion propagation from the inner ring to the chip, enhancing the resonator's isolation from the substrate.

The optimized N_r is 4, which maximizes the side beam length when all other parameters are the same. This trend shows that the optimized mode aimed to make the vibrating lateral beams as long as possible, as the quality factor of a string resonator[27] increases for a longer beam. Compared with the 1D approach,[14,15] which is a subset of our structure by considering $N_r = 2$, the web-like structure in the 2D domain has the potential to achieve higher Q_m by exploring novel soft-clamping motions compared to the limited number of vibration modes[16] of the 1D structure. The optimized l_2, which defines the distance between the centre and the inner radial beam, was close to the maximum limit, while the number of radial beams N_r was minimized. This trend shows that the optimized mode aimed to make the vibrating lateral beams as long as possible, as the quality factor of a string resonator[27] increases for a longer beam. Also, the w_2 was optimized at 1 μm which represents the minimum limit allowed. Allowing for widths thinner than 1 μm would likely increase the quality factor. While the lateral size, L, was limited to 3 mm, a study of increasing L (discussed in the Supporting Information) also shows that the optimized Q_m scales quadratically with the size of the resonator while f_m/Q_m is significantly reduced. All of these mechanisms work together to achieve a compact design with an ultrahigh quality factor at a lower-order vibration mode via a novel soft-clamping
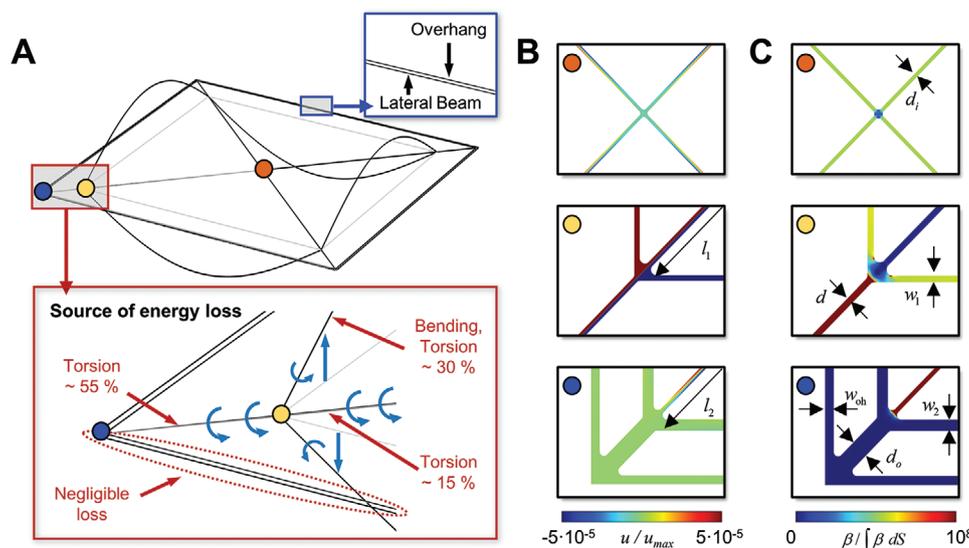

Figure 4. Optimized spiderweb design exhibiting a soft-clamping mode. A) The full motion of the optimized vibration mode shape with a zoom around the overhang and an illustration of the portion of energy loss. The gray part in this figure shows the structure at rest (no vibration). B) The local deformations and C) the normalized bending loss density for the three regions in (A). From top to bottom: center (orange marker), joint of the inner lateral beam (yellow marker), and the edge (blue marker).

approach that does not require the use of phononic crystals or sub-micrometer lithographic features. Notwithstanding, up to now this finding remains a computational prediction.

2.2. Experimental Results

While we have so far described the computational design process which occurred without experimental trial-and-error, the performance of the novel resonator needs to be experimentally validated. To do this we fabricate the optimal resonator and experimentally determine the quality factor of the system from a ringdown measurement in the ultrahigh-vacuum (UHV) setup shown in **Figure 5**F to avoid air damping. Ringdown measurements involve using piezoelectric stages to resonantly excite the motion of nanomechanical resonators, stopping the drive, and observing decay of the resonators' motion via interferometric optical readout. The rate of decay of the resonators amplitude gives its rate of energy dissipation and thus its mechanical quality factor. The spiderweb nanomechanical resonator is fabricated on high-stress Si_3N_4 grown by low-pressure chemical vapor deposition (LPCVD) on a silicon wafer (Figure 5A). The pattern is first written on a resist mask (Figure 5B), then transferred on the Si_3N_4 layer with a directional CHF_3 plasma etching (Figure 5C). After that, the resist mask is removed (Figure 5D) and the spiderweb nanomechanical resonator is suspended by a fluorine-based (SF_6) dry etching step (Figure 5E), which does not require any mask or additional cleaning steps, making the fabrication considerably easier, higher yield and higher quality. Crucially, this fabrication process allows for remarkable agreement between experimental results and idealized simulations

that allow us to reliably use the latter as data points for the machine-learning algorithm. A detailed explanation of the fabrication process and the mechanical characterization setup is summarized in the Experimental Section.

Figure 6A shows a scanning electron microscope image of the fabricated device, where the suspended Si_3N_4 spiderweb nanomechanical resonator is highlighted in blue, surrounded by dummy Si_3N_4 islands disconnected from the suspended structure, used to prevent overetching and overexposure (in light gray). The thermomechanical noise spectra as obtained by interferometric optical readout at the center of the spiderweb nanomechanical resonator (orange marker) and the inner lateral beam (pink marker) are plotted in Figure 6C. As shown in the figure, the optimal vibration mode occurring around 133.6 kHz is visible in the spectrum of the inner ring but has no amplitude in the center of the resonator and therefore well confined, contrary to the fundamental mode at 81.8 kHz. This corroborates the presence of the novel soft-clamping mode shown in Figure 4. Furthermore the simulated out-of-plane vibration mode frequencies agrees with experiments to around 1% as shown in Figure 6B. The presence of the torsional soft-clamping mode is further proved by the ringdown measurement shown in Figure 6D, where the quality factor of the optimized mode at 133.6 kHz is measured to be 1.8 billion, which is in excellent agreement with the computational predictions (1.75 billion) and the highest mechanical quality factor yet measured in this frequency range at room temperature. Compared to the fundamental mode's Q_m, it has more than 60 times higher value. In this research, we simulated the Q_m considering the dissipation dilution but the acoustic radiation (Q_{rad})[16,20] and the loss from gas damping (Q_{gas})[25] can also affect the ringdown in the
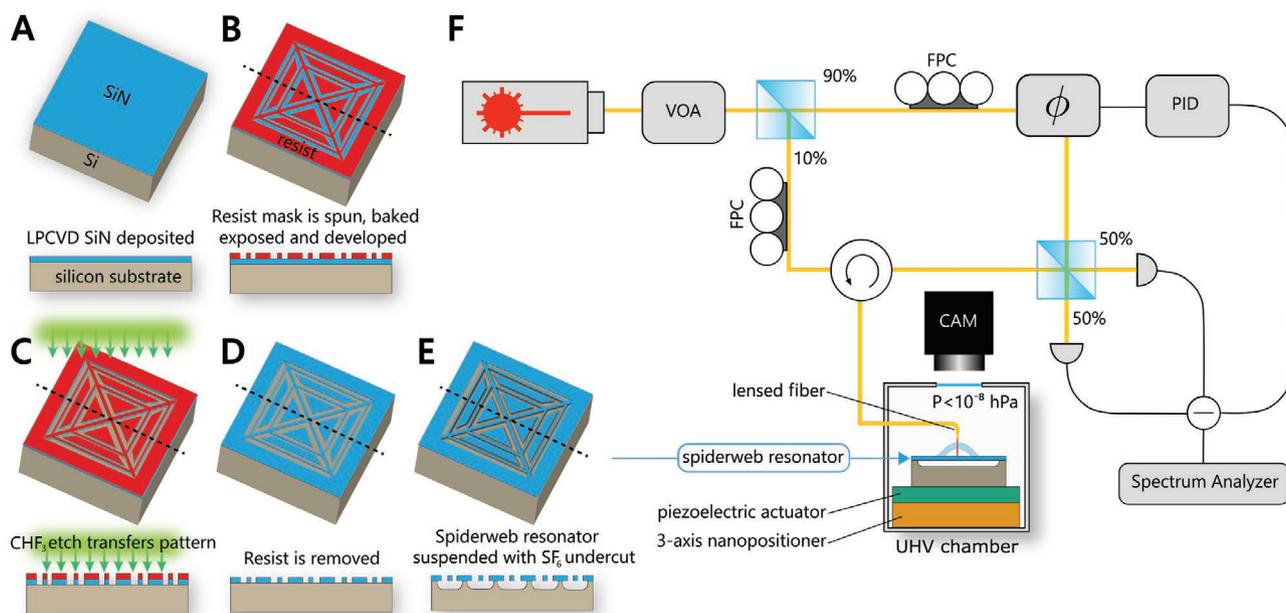

Figure 5. Schematic representation of the fabrication process flow and the mechanical characterization setup. A–E) Process steps consist of deposition of Si_3N_4 onto a silicon substrate (A), mask patterning (B), Si_3N_4 patterning via dry etching (C), mask removal (D), and Si_3N_4 undercut and release (E). F) The spiderweb nanomechanical resonator is resonantly driven by a piezoelectric actuator and its motion is optically measured with a balanced homodyne interferometer. The resonator is placed inside an UHV chamber to reach a pressure lower than 10^{-8} mbar. VOA, variable optical attenuator; PID, proportional integral derivative controller; FPC, fiber polarization controller; Φ, fiber stretcher.

**ADVANCED
SCIENCE NEWS**

www.advancedsciencenews.com

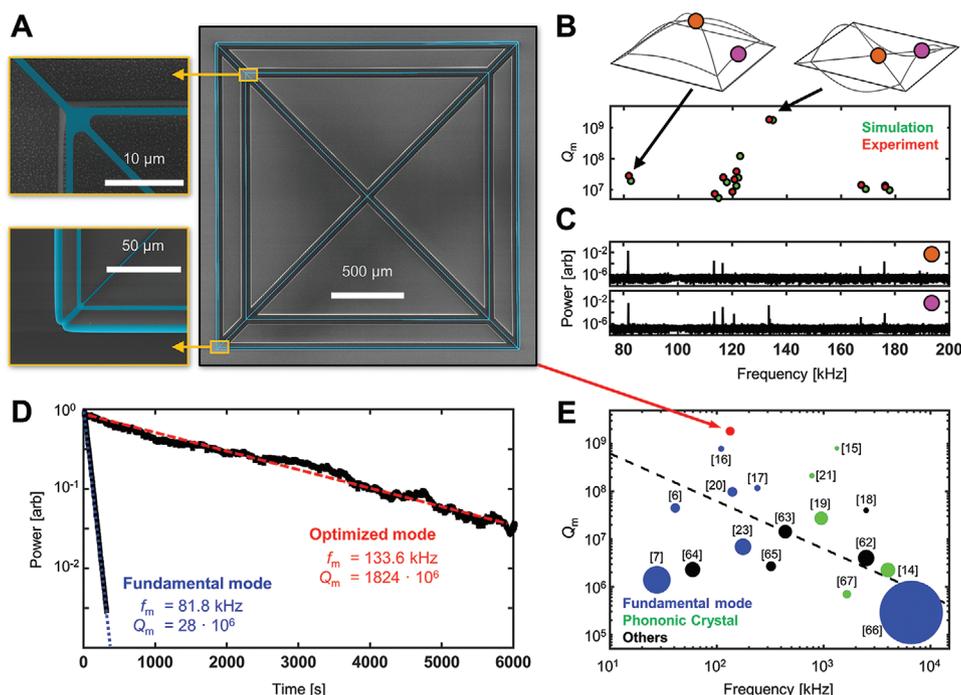**ADVANCED
MATERIALS**

www.advmat.de

Figure 6. Experimental characterization of the optimal spiderweb nanomechanical resonator. A) False-colored scanning electron microscopy images of the optimal design. B) Q_m from the simulation and experimental results of the out-of-plane vibration modes with the figure of the fundamental and optimized mode shapes. C) The thermomechanical noise spectra measured at the center of the resonator (orange marker) and at the center of the inner lateral beam (pink marker). The y axis is the normalized power with respect to the maximum power. D) Ringdown measurement of the optimized 3 mm spiderweb resonator excited in its 133.6 kHz mode with an extracted quality factor higher than 1.8 billion, compared with the quality factor measured for the fundamental mode at 81.8 kHz. The y axis is the normalized power with respect to the power at time = 0 for each curve. E) Comparison of the presented experiment result with state-of-the-art experiment reports.[6,7,14–21,23,62–67] Marker area corresponds to their aspect ratio t/L. The dashed line corresponds to the mechanical decoherence constraint in Figure 1

experiment. The excellent match between bending loss simulations and experimental results supports our hypothesis that bending loss is the dominant source of mechanical loss for the spiderweb nanomechanical resonator. While acoustic radiation loss (through the substrate) affects mechanical resonators with motion near the resonator–substrate boundary,[16,17,20] it is expected to be negligible in our optimal design because the resonator motion is isolated from the substrate, with the support of the outer lateral beams, as described in Figure 4. At the same time, the gas damping effect can be ignored by performing the measurement under a sufficiently high vacuum of 4.0×10^{-9} hPa. The high Q_m result is especially striking when considering the short length and larger thickness of the resonator than existing solutions in the literature, making it more practical to fabricate and operate. Figure 6E compares our result with the state-of-the-art nanomechanical resonator's experiment values at room temperature by plotting their Q_m, f_m, and their aspect ratio t/L via marker area when t and L represent the thickness and the size of each reported resonator, respectively. It supports that our spiderweb resonator has obtained a high Q_m not using more challenge fabrication but considering novel vibration mode.

3. Conclusion

A simulation-based data-driven optimization approach was used to design a spiderweb nanomechanical resonator with

ultralow dissipation in room-temperature environments. Our approach relies on the observation that spiderwebs have evolved over millions of years through evolutionary competition to be remarkable vibration sensors.[29,30] Using silicon nitride as a base material, our machine-learning algorithm hitchhikes on this natural optimization, and discovers nanomechanical designs tailored for high-precision sensors. While silicon nitride is one of the most widely used thin films for nanomechanical resonators, the design approach in this work could be extended to other materials such as diamond,[68] gallium arsenide,[64,69] silicon carbide,[70,71] indium gallium phosphide,[65,72] fused silica glass,[73] silicon,[74] phosphorus carbide,[75,76] and even superconducting films.[77,78] The enhancement of mechanical quality factor results from the discovery of a soft-clamping mechanism that uses a torsional motion to isolate a nanomechanical mode from ambient thermal noise. This enables high-Q_m nanomechanical resonators that have smaller aspect ratios than previous state-of-the-art designs, making them significantly easier, cheaper, and faster to manufacture. Our experimental validation demonstrates a new class of mechanical resonators that exhibit mechanical quality factor exceeding a billion in room-temperature environments. This is achieved via a torsional soft-clamping mechanism that avoids radiation losses without using phononic crystals or submicrometer lithographic features. While other state-of-the-art resonators require tethers which are hundreds of nanometers in width, our resonators (with micrometer-sized features) can

2106248 (8 of 11)

be reliably fabricated at large scales with photolithography. While high-Q_m resonators typically require $\approx$20–30 nm thicknesses, we design ours with 50 nm thickness to simplify the fabrication. Undoubtedly, by designing our resonators tethers with sub-micrometer tethers and thinner geometries, we could further improve Q_m at the cost of making the fabrication less accessible for general use. The low dissipation rate of the resonator, with $f_m/Q_m \approx 75$ µHz, also represents an important step toward high-precision sensing applications and room-temperature quantum technologies. This includes quantum-limited force microscopy,[2] "cavity-free" cooling scheme[79] and quantum control of motion at room temperature.[80] What is fascinating is that the machine-learning algorithm independently hones in on torsional vibration mechanisms, which are actually used by spiderwebs in nature when detecting prey, although the algorithm does not have any prior knowledge of how a spiderweb functions. Notwithstanding, we recognize that this data-driven exploration guided by machine learning is just a first step toward rational design of the next generation of nanomechanical resonators. The demonstrated approach for realizing high-Q_m resonance modes is not restricted to the specific spiderweb-like design studied in this work. The design strategy might be applied to a wide range of geometries and design problems involving low-throughput simulations or experiments (the most common scenario in engineering and science). We expect future developments in machine learning and optimization together with novel fabrication techniques to lead to unprecedented nanotechnology within the next decade.

4. Experimental Section

Fabrication Process: The nanomechanical resonators were fabricated from 58 nm-thick high-stress (1.07 GPa) Si_3N_4 deposited by LPCVD on a silicon substrate (Figure 5A). The disposition was carried out in-house, which allowed to obtain Si_3N_4 films of arbitrary thickness in stoichiometric form (3/4 ratio of silicon to nitrogen) leading to the uniform high tensile stress in the film. The pattern in the resonator was first written in a positive tone resist (AR-P 6200) by electron beam lithography (Figure 5B) to create a mask. To do so, the resist was spin coated on top of the Si_3N_4, baked at 155 °C, exposed and developed in pentylacetate. Note that e-beam lithography was used instead of optical lithography due to the high level of control and flexibility for the device geometry which was highly beneficial during the development of a new design. However the minimum features of the resonators were designed to be 1 µm to ensure a easier, large-scale fabrication with optical lithography. The pattern was then transferred into the silicon nitride thin-film layer using an inductively coupled plasma (ICP) etching based on a CHF_3 plasma etch (Figure 5C). Next, the resist was removed with dimethylformamide followed by two cleaning steps with hot piranha solution to remove organic residues and diluted hydrofluoric acid solution to remove surface oxides (Figure 5D). Last, the Si_3N_4 layer was released from the silicon substrate with an ICP etching with SF_6 at −120 °C (Figure 5E),[81] performed at high pressure and low DC bias to etch isotropically the silicon substrate. This last step did not require any mask given the high selectivity of the chosen chemical against silicon nitride, avoiding any additional cleaning steps and removing any limitation posed by capillary force or stiction usually encountered in isotropic wet etchings (such as potassium hydroxide, KOH, or tetramethylammonium hydroxide, TMAH). Moreover, it was not constrained by the crystal planes of the silicon substrate, enabling the fabrication of arbitrary shapes and avoiding multiple exposures. The final thickness of the Si_3N_4 films was expected to be 50 nm.

Mechanical Characterization Setup: All the measurements presented were performed using a custom balanced homodyne detection interferometer (Figure 5F). The mechanical displacement was probed with a fiber coupled infrared laser (1550 nm). The power was divided into two arms: the local oscillator (90%) used as interference reference and the signal arm (10%) terminated with a lensed fiber. The signal arm and the device were mounted on two separate 3-axis nanopositioners placed perpendicular to each other, in order to align the device to the focal plane of the lensed fiber. In this way the signal which came out from the lensed fiber was focused on the device and its reflection was collected back inside the fiber. A piezoelectric plate was connected to the sample holder to actuate the devices mechanically. To reduce the effect of gas damping on the measurements, the lensed fiber and sample stage were placed inside a vacuum chamber. With the aid of a turbomolecular and a diaphragm pump, the system can reach a pressure of 4.0×10^{-9} hPa. The sensitivity of the measured signal to phase oscillations was maximal in the linear region of the interference signal. To this end, the phase of the local oscillator signal was controlled with a fiber stretcher driven by a proportional integral derivative (PID) controller implemented with a field-programmable gate array (FPGA) board (RedPitaya 125-14) in order to stabilize the interferometer's low frequency fluctuations using the signal measured from the balanced photodetector as an error signal for a feedback loop. Thermomechanical noise spectra were acquired with an electronic spectrum analyzer without mechanical excitation applied to the piezoelectric plate. On the contrary, for the ringdown measurements the device was first actuated close to the mechanical resonance frequency of interest with the piezoelectric plate until it reached and excited steady state. Second, the mechanical actuation was turned off and the decay in time of the measured displacement signal was measured with an electronic spectrum analyzer by setting a resolution bandwidth larger than 5 Hz. The bandwidth needed to be larger than the expected linewidth of the resonator, but small enough to increase the signal-to-noise ratio.

Supporting Information

Supporting Information is available from the Wiley Online Library or from the author.

Acknowledgements

Conflict of Interest

The authors declare no conflict of interest.

**ADVANCED
SCIENCE NEWS**

www.advancedsciencenews.com

**ADVANCED
MATERIALS**

www.advmat.de

[1] F. Marquardt, J. P. Chen, A. A. Clerk, S. Girvin, *Phys. Rev. Lett.* **2007**, *99*, 093902.

[2] D. Hälg, T. Gisler, Y. Tsaturyan, L. Catalini, U. Grob, M. Krass, M. H'eritier, H. Mattiat, A. Thamm, R. Schirhagl, E. Langman, A. Schliesser, C. Degen, A. Eichler, *Physical Review Applied* **2021**, *15*, L021001.

[3] M. Metcalfe, *Appl. Phys. Rev.* **2014**, *1*, 031105.

[4] M. A. Page, M. Goryachev, H. Miao, Y. Chen, Y. Ma, D. Mason, M. Rossi, C. D. Blair, L. Ju, D. G. Blair, A. Schliesser, M. E. Tobar, C. Zhao, *Commun. Phys.* **2021**, *4*, 27.

[5] A. H. Safavi-Naeini, O. Painter, *New J. Phys.* **2011**, *13*, 013017.

[6] C. Reinhardt, T. Müller, A. Bourassa, J. C. Sankey, *Phys. Rev. X* **2016**, *6*, 021001.

[7] A. G. Krause, M. Winger, T. D. Blasius, Q. Lin, O. Painter, *Nat. Photonics* **2012**, *6*, 768.

[8] D. Carney, G. Krnjaic, D. Moore, C. Regal, G. Afek, S. Bhave, B. Brubaker, T. Corbitt, J. Cripe, N. Crisosto, A. Geraci, S. Ghosh, J. G. E. Harris, A. Hook, E. Kolb, J. Kunjummen, R. Lang, T. Li, T. Lin, Z. Liu, J. Lykken, L. Magrini, J. Manley, N. Matsumoto, A. Monte, F. Monteiro, T. Purdy, C. J. Riedel, R. Singh, S. Singh, K. Sinha, J. M. Taylor, J. Qin, D. J. Wilson, Y. Zhao, *Quantum Sci. Technol.* **2021**, *6*, 024002.

[9] J. Manley, M. D. Chowdhury, D. Grin, S. Singh, D. J. Wilson, *Phys. Rev. Lett.* **2021**, *126*, 061301.

[10] J. Schmöle, M. Dragosits, H. Hepach, M. Aspelmeyer, *Class. Quantum Gravity* **2016**, *33*, 125031.

[11] H. Miao, D. Martynov, H. Yang, A. Datta, *Phys. Rev. A* **2020**, *101*, 063804.

[12] J. Chan, T. M. Alegre, A. H. Safavi-Naeini, J. T. Hill, A. Krause, S. Gröblacher, M. Aspelmeyer, O. Painter, *Nature* **2011**, *478*, 89.

[13] U. Delić, M. Reisenbauer, K. Dare, D. Grass, V. Vuletić, N. Kiesel, M. Aspelmeyer, *Science* **2020**, *367*, 892.

[14] A. H. Ghadimi, D. J. Wilson, T. J. Kippenberg, *Nano Lett.* **2017**, *17*, 3501.

[15] A. H. Ghadimi, S. A. Fedorov, N. J. Engelsen, M. J. Bereyhi, R. Schilling, D. J. Wilson, T. J. Kippenberg, *Science* **2018**, *360*, 764.

[16] A. Beccari, M. J. Bereyhi, R. Groth, S. A. Fedorov, A. Arabmoheghi, N. J. Engelsen, T. J. Kippenberg, arXiv: 2103.09785, **2021**.

[17] D. Høj, F. Wang, W. Gao, U. B. Hoff, O. Sigmund, U. L. Andersen, *Nat. Commun.* **2021**, *12*, 5766.

[18] S. Chakram, Y. Patil, L. Chang, M. Vengalattore, *Phys. Rev. Lett.* **2014**, *112*, 127201.

[19] J. Guo, R. Norte, S. Gröblacher, *Phys. Rev. Lett.* **2019**, *123*, 223602.

[20] R. A. Norte, J. P. Moura, S. Gröblacher, *Phys. Rev. Lett.* **2016**, *116*, 147202.

[21] Y. Tsaturyan, A. Barg, E. S. Polzik, A. Schliesser, *Nat. Nanotechnol.* **2017**, *12*, 776.

[22] S. A. Fedorov, A. Beccari, N. J. Engelsen, T. J. Kippenberg, *Phys. Rev. Lett.* **2020**, *124*, 025502.

[23] S. Schmid, K. Jensen, K. Nielsen, A. Boisen, *Phys. Rev. B* **2011**, *84*, 165307.

[24] S. S. Verbridge, J. M. Parpia, R. B. Reichenbach, L. M. Bellan, H. G. Craighead, *J. Appl. Phys.* **2006**, *99*, 124304.

[25] S. Schmid, C. Hierold, *J. Appl. Phys.* **2008**, *104*, 093516.

[26] B. Zwickl, W. Shanks, A. Jayich, C. Yang, A. Bleszynski Jayich, J. Thompson, J. Harris, *Appl. Phys. Lett.* **2008**, *92*, 103125.

[27] S. A. Fedorov, N. J. Engelsen, A. H. Ghadimi, M. J. Bereyhi, R. Schilling, D. J. Wilson, T. J. Kippenberg, *Phys. Rev. B* **2019**, *99*, 054107.

[28] W. Gao, F. Wang, O. Sigmund, *Comput. Methods Appl. Mech. Eng.* **2020**, *361*, 112692.

[29] S. W. Cranford, A. Tarakanova, N. M. Pugno, M. J. Buehler, *Nature* **2012**, *482*, 72.

[30] R. Zaera, A. Soler, J. Teus, *J. R Soc. Interface* **2014**, *11*, 20140484.

[31] J. Jyoti, A. Kumar, P. Lakhani, N. Kumar, B. Bhushan, *Philos. Trans. R. Soc. A* **2019**, *377*, 20180271.

[32] F. Vollrath, *Sci. Am.* **1992**, *266*, 70.

[33] J. Gosline, P. Guerette, C. Ortlepp, K. Savage, *J. Exp. Biol.* **1999**, *202*, 3295.

[34] C. Boutry, T. A. Blackledge, *Zoology* **2009**, *112*, 451.

[35] A. Meyer, N. M. Pugno, S. W. Cranford, *J. R. Soc., Interface* **2014**, *11*, 20140561.

[36] W. M. Masters, *Behav. Ecol. Sociobiol.* **1984**, *15*, 207.

[37] N. Du, Z. Yang, X. Y. Liu, Y. Li, H. Y. Xu, *Adv. Funct. Mater.* **2011**, *21*, 772.

[38] W. M. Barrows, *Biol. Bull.* **1915**, *29*, 316.

[39] B. Mortimer, C. Holland, J. F. Windmill, F. Vollrath, *J. R. Soc. Interface* **2015**, *12*, 20150633.

[40] H. Gao, B. Ji, I. L. Jäger, E. Arzt, P. Fratzl, *Proc. Natl. Acad. Sci. U. S. A.* **2003**, *100*, 5597.

[41] J. Aizenberg, J. C. Weaver, M. S. Thanawala, V. C. Sundar, D. E. Morse, P. Fratzl, *Science* **2005**, *309*, 275.

[42] S. Kamat, X. Su, R. Ballarini, A. Heuer, *Nature* **2000**, *405*, 1036.

[43] M. Miniaci, A. Krushynska, A. B. Movchan, F. Bosia, N. M. Pugno, *Appl. Phys. Lett.* **2016**, *109*, 071905.

[44] A. Krushynska, F. Bosia, M. Miniaci, N. Pugno, *New J. Phys.* **2017**, *19*, 105001.

[45] X. Liu, D. Liu, J. hun Lee, Q. Zheng, X. Du, X. Zhang, H. Xu, Z. Wang, Y. Wu, X. Shen, J. Cui, Y. Mai, J.-K. Kim, *ACS Appl. Mater. Interfaces* **2018**, *11*, 2282.

[46] P.-L. Yu, T. Purdy, C. Regal, *Phys. Rev. Lett.* **2012**, *108*, 083603.

[47] L. G. Villanueva, S. Schmid, *Phys. Rev. Lett.* **2014**, *113*, 227201.

[48] G. X. Gu, C.-T. Chen, D. J. Richmond, M. J. Buehler, *Mater. Horiz.* **2018**, *5*, 939.

[49] J. Carrasquilla, R. G. Melko, *Nat. Phys.* **2017**, *13*, 431.

[50] P. Jiao, A. H. Alavi, *Appl. Mater. Today* **2020**, *21*, 100816.

[51] Y. Ding, M. Kim, S. Kuindersma, C. J. Walsh, *Sci. Rob.* **2018**, *3*, 15.

[52] R. Shalloo, S. Dann, J.-N. Gruse, C. Underwood, A. Antoine, C. Arran, M. Backhouse, C. Baird, M. Balcazar, N. Bourgeois, J. A. Cardarelli, P. Hatfield, J. Kang, K. Krushelnick, S. Mangles, C. Murphy, N. Lu, J. Osterhoff, K. Põder, P. Rajeev, C. Ridgers, S. Rozario, M. Selwood, A. Shahani, D. Symes, A. Thomas,

2106248 (10 of 11)

**ADVANCED
SCIENCE NEWS**

www.advancedsciencenews.com

**ADVANCED
MATERIALS**

www.advmat.de

C. Thornton, Z. Najmudin, M. Streeter, *Nat. Commun.* **2020**, *11*, 6355.

[53] B. J. Shields, J. Stevens, J. Li, M. Parasram, F. Damani, J. I. M. Alvarado, J. M. Janey, R. P. Adams, A. G. Doyle, *Nature* **2021**, *590*, 89.

[54] M. Pelikan, D. E. Goldberg, E. Cantú-Paz in *GECCO'99: Proc. 1st Annu. Conf. on Genetic and Evolutionary Computation*, Vol. *1*, Morgan Kaufmann Publishers Inc., San Francisco, CA, USA **1999**, pp. 525–532.

[55] M. A. Bessa, P. Glowacki, M. Houlder, *Adv. Mater.* **2019**, *31*, 1904845.

[56] P. I. Frazier, J. Wang, *Information Science for Materials Discovery and Design*, Springer, Berlin, Germany **2016**, pp. 45–75.

[57] B. Shahriari, K. Swersky, Z. Wang, R. P. Adams, N. De Freitas, *Proc. IEEE* **2015**, *104*, 148.

[58] The-GPyOpt-authors, Gpyopt: A Bayesian Optimization Framework in Python, http://github.com/SheffieldML/GPyOpt (accessed: May 2021).

[59] Introduction to COMSOL Multiphysics, COMSOL, Inc. Burlington, MA, USA **2018**.

[60] A. Kawano, A. Morassi, *SIAM J. Appl. Math.* **2019**, *79*, 2506.

[61] J. Steinlechner, C. Krüger, I. W. Martin, A. Bell, J. Hough, H. Kaufer, S. Rowan, R. Schnabel, S. Steinlechner, *Phys. Rev. D* **2017**, *96*, 022007.

[62] D. J. Wilson, C. A. Regal, S. B. Papp, H. Kimble, *Phys. Rev. Lett.* **2009**, *103*, 207204.

[63] E. Serra, B. Morana, A. Borrielli, F. Marin, G. Pandraud, A. Pontin, G. A. Prodi, P. M. Sarro, M. Bonaldi, *J. Microelectromech. Syst.* **2018**, *27*, 1193.

[64] K. Usami, A. Naesby, T. Bagci, B. M. Nielsen, J. Liu, S. Stobbe, P. Lodahl, E. S. Polzik, *Nat. Phys.* **2012**, *8*, 168.

[65] G. D. Cole, P.-L. Yu, C. Gärtner, K. Siquans, R. Moghadas Nia, J. Schmöle, J. Hoelscher-Obermaier, T. P. Purdy, W. Wieczorek, C. A. Regal, M. Aspelmeyer, *Appl. Phys. Lett.* **2014**, *104*, 201908.

[66] T. Faust, P. Krenn, S. Manus, J. P. Kotthaus, E. M. Weig, *Nat. Commun.* **2012**, *3*, 728.

[67] C. Reetz, R. Fischer, G. G. Assumpcao, D. P. McNally, P. S. Burns, J. C. Sankey, C. A. Regal, *Phys. Rev. Appl.* **2019**, *12*, 044027.

[68] Y. Nakamura, S. Sakagami, Y. Amamoto, Y. Watanabe, *Thin Solid Films* **1997**, *308*, 249.

[69] J. Liu, K. Usami, A. Naesby, T. Bagci, E. S. Polzik, P. Lodahl, S. Stobbe, *Appl. Phys. Lett.* **2011**, *99*, 243102.

[70] A. R. Kermany, G. Brawley, N. Mishra, E. Sheridan, W. P. Bowen, F. Iacopi, *Appl. Phys. Lett.* **2014**, *104*, 081901.

[71] E. Romero, V. M. Valenzuela, A. R. Kermany, L. Sementilli, F. Iacopi, W. P. Bowen, *Phys. Rev. Appl.* **2020**, *13*, 044007.

[72] M. Bückle, V. C. Hauber, G. D. Cole, C. Gärtner, U. Zeimer, J. Grenzer, E. M. Weig, *Appl. Phys. Lett.* **2018**, *113*, 201903.

[73] A. Cumming, B. Sorazu, E. Daw, G. Hammond, J. Hough, R. Jones, I. Martin, S. Rowan, K. Strain, D. Williams, *Class. Quantum Gravity* **2020**, *37*, 195019.

[74] A. Beccari, D. A. Visani, S. A. Fedorov, M. J. Bereyhi, V. Boureau, N. J. Engelsen, T. J. Kippenberg, arXiv: 2107.02124, **2021**.

[75] W. C. Tan, Y. Cai, R. J. Ng, L. Huang, X. Feng, G. Zhang, Y.-W. Zhang, C. A. Nijhuis, X. Liu, K. Ang, *Adv. Mater.* **2017**, *29*, 1700503.

[76] A. A. Kistanov, V. R. Nikitenko, O. V. Prezhdo, *J. Phys. Chem. Lett.* **2021**, *12*, 620.

[77] D. T. Read, Y.-W. Cheng, R. R. Keller, J. D. McColskey, *Scr. Mater.* **2001**, *45*, 583.

[78] M. Nahar, N. Rocklein, M. Andreas, G. Funston, D. Goodner, *J. Vac. Sci. Technol., A* **2017**, *35*, 01B144.

[79] C. M. Pluchar, A. R. Agrawal, E. Schenk, D. J. Wilson, *Appl. Opt.* **2020**, *59*, G107.

[80] M. Rossi, D. Mason, J. Chen, Y. Tsaturyan, A. Schliesser, *Nature* **2018**, *563*, 53.

[81] R. A. Norte, M. Forsch, A. Wallucks, I. Marinković, S. Gröblacher, *Phys. Rev. Lett.* **2018**, *121*, 030405.